J. Fluid Mech. (2021), *vol*. 915, A52, doi:10.1017/jfm.2021.123

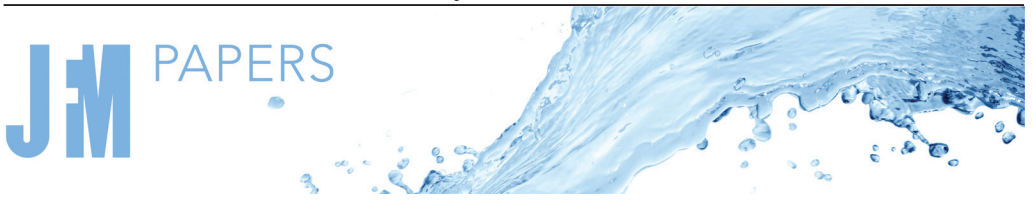

Water impact of a surface-patterned disk

Taehyun Kim[1], **Donghyun Kim**[1] **and Daegyoum Kim**[1],†

[1]Department of Mechanical Engineering, KAIST, Daejeon 34141, Republic of Korea

(Received 13 April 2020; revised 17 November 2020; accepted 4 February 2021)

This study experimentally investigates the effect of a surface pattern applied to a flat disk on the impact force during water entry. A macroscale mesh-like pattern with square holes is applied to the bottom surface of a flat disk, and the shape of the pattern and the falling speed of the disk are varied to find a universal parameter that characterizes the impact force. When a surface-patterned disk impacts a free surface, air is trapped inside the holes, and the subsequent compression and depressurization of the trapped air is accompanied by a rise and fall in the impact force. Under the cushioning effect of the trapped air, the peak of the impact force decreases and its period extends as the total volume of holes in the surface pattern increases. These changes are independent of the specific shape of the pattern. In contrast, the impulse exerted on the disk remains similar, regardless of the total volume of holes and the pattern. We conduct a simple theoretical analysis based on the added mass of the disk to estimate the impact force, and confirm the trends observed in our experiments.

Key words: interfacial flows (free surface)

1. Introduction

The impact of a solid object on a free surface is of importance in ocean engineering, with examples including ship slamming (Abrate 2011; Kapsenberg 2011), air-to-sea missiles (May 1975), free-fall lifeboats (Ringsberg *et al.* 2017) and surface-piercing propellers (Yari & Ghassemi 2016). The impact of a solid body on water is also observed in nature. Basilisk lizards, as well as western and Clark's grebes, support their weight as they run on water by quickly slapping their feet on the water surface (Glasheen & McMahon 1996*a*; Hsieh & Lauder 2004; Clifton, Hedrick & Biewener 2015). Birds such as northern gannets and kingfishers dive into water to catch prey (Chang *et al.* 2016; Crandell, Howe & Falkingham 2019). These interesting biological behaviours have inspired the development of water-running robots and shape-morphing aerial unmanned vehicles (Floyd *et al.* 2006; Floyd & Sitti 2008; Siddall, Ortega Ancel & Kovač 2017).

† Email address for correspondence: daegyoum@kaist.ac.kr

Because of rich fluid dynamics, the vertical impact of a solid object, primarily a sphere, on the air–water interface has been studied extensively; for a review of the relevant literature, see Truscott, Epps & Belden (2014). For example, at the initial moment of impact, a horizontal jet with a velocity of up to 30 times the impact speed is formed (Thoroddsen *et al.* 2004). For sufficiently large impact speeds, when a sphere continues to descend below the free surface after impact, air is entrained behind the sphere, forming an air cavity (Duez *et al.* 2007). The air cavity eventually pinches off near the free surface or midway to the sphere (Aristoff & Bush 2009), and simultaneously a splash curtain appears on the free surface (Marston *et al.* 2016). These phenomena also occur for other geometries, such as wedges (Vincent *et al.* 2018) and disks (Bergmann *et al.* 2009; Gekle & Gordillo 2010).

These complex fluid behaviours are closely related to the unsteady hydrodynamic force exerted on an impacting solid object (Truscott, Epps & Techet 2012; Wang, Faltinsen & Lugni 2019). Since the pioneering work of Wagner (1932), there have been significant efforts to analyse the force that arises shortly after the free-surface impact. A variety of analytical and numerical models based on potential flow theory have been proposed for the impact force of the early phase; see Korobkin & Pukhnachov (1988) and references therein. It is widely accepted that the impact force of the early phase is due to the added-mass effect whereby the initially quiescent pool of water is accelerated by the entering object (Korobkin & Pukhnachov 1988). Later, researchers used the matched asymptotic expansion (Howison, Ockendon & Wilson 1991), nonlinear boundary element method (Zhao & Faltinsen 1993), or higher-order terms in the Bernoulli equation (Korobkin 2004) to better predict the pressure associated with slamming wedges. Recently, the Euler–Bernoulli beam theory was used to build a semianalytical model for a flexible wedge entering the free surface (Shams & Porfiri 2015). In addition to theoretical studies, experimental measurements of the impact force have been conducted. Multiple pressure transducers were used to determine the pressure distribution on the surface of a wedge, with a successive rise in pressure found to be accompanied by the climbing of water along the wedge (Yettou, Desrochers & Champoux 2006). Rather than using the pressure distribution, the impact force on the body was directly measured using a force sensor. It was revealed that the maximum impact force upon water entry occurs before the submergence of one body length for both spheres (Moghisi & Squire 1981) and wedges (Vincent *et al.* 2018). The pressure field on the surface of a wedge has also been reconstructed from the velocity field obtained by particle image velocimetry (Jalalisendi *et al.* 2015; Shams, Jalalisendi & Porfiri 2015).

In contrast to a wedge or sphere, solid structures with a flat bottom surface, such as plates or disks, do not gradually become wet during water entry. Instead, the entire bottom surface impacts the water within a very short duration, and the pressure rises simultaneously over the entire bottom surface, which results in a steep peak in the impact force. Experiments conducted by Ma *et al.* (2016) showed that a plate impacting a free surface incurs a peak pressure at its centre and approximately half this value near its edge. Interestingly, for a structure with a flat bottom, a thin layer of air is trapped between the flat bottom and the water surface (Verhagen 1967; Ermanyuk & Ohkusu 2005; Mayer & Krechetnikov 2018). By virtue of the trapped air, the peak pressure for a flat plate, as measured experimentally, is smaller than the value predicted theoretically in the absence of air, which is known as the air-cushioning effect (Verhagen 1967). This air-cushioning effect has been quantified for a disk impacting shallow water by comparing the impulsive motion of a floating disk and a free-falling disk (Ermanyuk & Ohkusu 2005). The impact load acquired by the pressure probe is smaller for the free-falling disk as a result of the air-cushioning effect. Furthermore, Okada & Sumi (2000) measured the pressure on an impacting plate by

varying the inclination angle with respect to the free surface from 0° to 4°, and showed that the air-cushioning effect starts to diminish at a specific inclination angle.

Strong hydrodynamic loading during the early phase of water impact may cause severe damage to a structure. To reduce the peak impact force and thus prevent structural damage, several approaches have been proposed for wedges, slender bodies and flat plates. For wedges, the impact force decreases as the wedge angle becomes smaller (Vincent *et al.* 2018). Regarding axisymmetric slender bodies with different nose geometries pointing downward, those with ogive noses experience much smaller impact forces than those with flat noses (Bodily, Carlson & Truscott 2014). Mathai, Govardhan & Arakeri (2015) reported a reduction in peak pressure with a concave-nosed body, the result of air trapped inside the concave hole. In addition to a change in object shape, the conditions surrounding an impacting object were varied. For a sphere placed inside a downward columnar jet of water, so that the sphere and water jet fall together into a quiescent pool of water, the impact force on the sphere is less than that of a sphere falling without a water jet (Speirs *et al.* 2019). The peak pressure on a plate impacting aerated water is much smaller than that impacting still water, because air bubbles extend the period over which shock loading is applied to the plate (Ma *et al.* 2016). The presence of a cylinder underneath the free surface also induces a pressure drop in the pileup region of an impacting wedge (Jalalisendi, Benbelkacem & Porfiri 2018).

In this study, we introduce another approach for reducing the peak impact force for a solid object with a flat bottom surface: a disk with a macroscale mesh-like surface pattern. The use of the mesh-like pattern as a means of lowering the peak of the hydrodynamic loading has, to the best of our knowledge, not previously been reported. From measurements of the impact force obtained with a force sensor, we analyse which geometrical parameters of the surface pattern are critical in determining the impact force, and identify the underlying physical mechanisms by examining the fluid behaviour underneath the pattern using high-speed visualization. To support our arguments, theoretical analysis is also conducted in order to predict the force at the instant of water entry. Although microscale surface patterning that alters the wettability of the surface is expected to be ineffective in diminishing the impact force of a flat-bottomed surface (Bodily *et al.* 2014), the application of a macroscale surface pattern may lead to a significant reduction in the impact force.

2. Experimental set-up

A water tank of dimensions 45 cm × 60 cm × 45 cm was filled with tap water to a depth of 32 cm for the water entry of a surface-patterned disk. The disk was initially held by an electromagnet and then released to fall freely (figure 1*a*). The disk was attached to a long rectangular rigid rod of length 25 cm, which was connected to a force sensor (Mini40 IP68, ATI Industrial Automation, Inc.). The force sensor was mounted beneath a long rigid bar that was parallel to the free surface (black-dashed box in figure 1*a*, falling unit). The impact speed U is defined as the velocity of the disk at the moment of impact upon the free surface, calculated as $U = (2gH)^{1/2}$, where H is the initial height of the disk bottom above the free surface. After impacting the free surface, a bumper prevented the disk from hitting the bottom of the water tank; the bumper does not affect the measurement of the impact force.

For a mesh-like surface pattern, disks of thickness $h = 2$, 3 and 4 mm and diameter $D = 30$ and 50 mm were laser cut from an acrylic plate and perforated with square holes (figure 1*b*). Here, the edge of the disk remained as a rim of 2 mm to enclose the surface pattern. Different surface patterns were obtained by varying the size d of the square holes

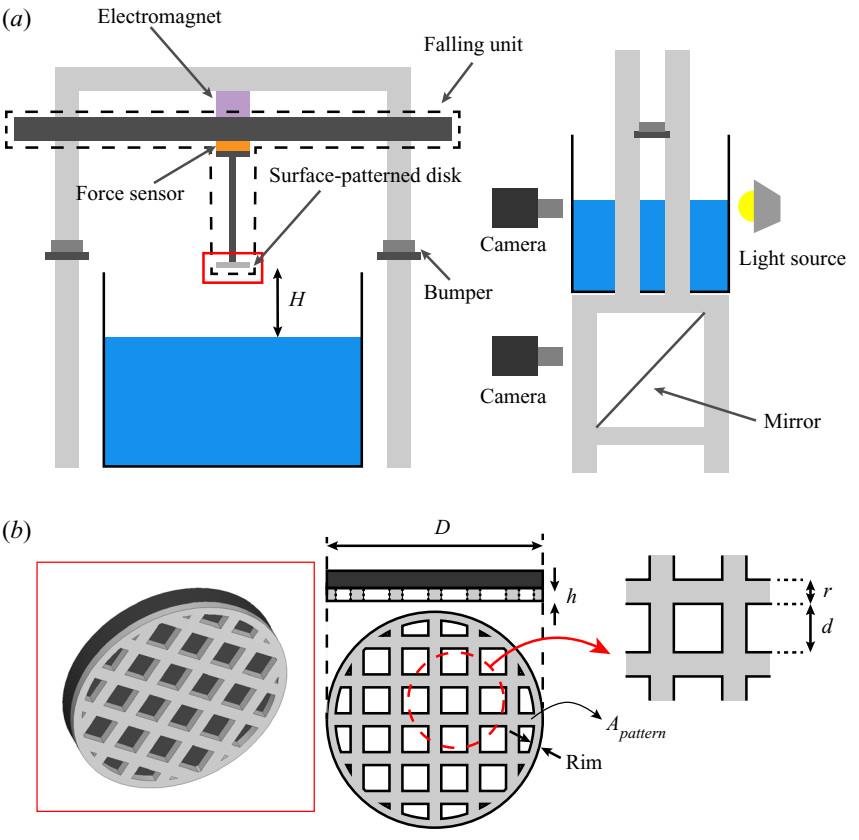

Figure 1. (*a*) Schematic diagram of experimental set-up. (*b*) Geometry of a surface-patterned disk. Square holes on the disk are positioned regularly with an identical distance r between the holes.

and the distance r between the holes. The distance r was chosen to be either 1.8, 2.8 or 3.8 mm, and the hole size d was selected such that the ratio d/r varied in the range 0.5–6. The perforated disk (grey part in figure 1*b*) was then bonded to a flat acrylic disk of the same diameter (black part in figure 1*b*) to produce a surface-patterned disk. The total thickness of the perforated disk and the flat disk was kept constant as 7 mm for all experimental cases. The dimensions and impact speeds of the surface-patterned disks are listed in table 1.

The impact force was measured by the force sensor, with signals acquired through a data acquisition board (PCIe-6321, National Instruments) at a sampling rate of 40 kHz. At the moment of impact, a high-speed camera (FASTCAM SA-Z, Photron, Inc.) recorded images at 20 000 frames per second. The camera captured the front and bottom views of the impacting disk and the surrounding air–water interface. For the bottom view, a mirror was placed under the water tank, and a reflected image was recorded (figure 1*a*). The force sensor and the camera were synchronized so that the generation of the impact force could be related to the fluid behaviour beneath the disk.

3. Results and discussion

3.1. *Reduction in impact force*

A body falling on a free surface experiences an impact force that peaks for a short duration. General force profiles for a flat disk (without a surface pattern) and a surface-patterned

D (mm)	r (mm)	d (mm)	h (mm)	U (m s^{-1})
50	1.8	2.2, 4.2, 6.2, 8.2, 10.2	2	1.71
50	2.8	2.2, 3.2, 6.2, 9.2, 12.2, 15.2	2	1.71
50	3.8	2.2, 4.2, 6.2, 8.2, 10.2, 12.2, 14.2, 16.2	2	1.71
50	1.8	2.2, 4.2, 6.2, 8.2, 10.2	2	0.99
30	1.8	2.2, 4.2, 6.2	2	1.71
30	2.8	2.2, 3.2, 6.2	2	1.71
30	3.8	2.2, 4.2	2	1.71
30	1.8	2.2, 4.2, 6.2	2	2.21
30	2.8	2.2, 3.2, 6.2	2	2.21
30	3.8	2.2, 4.2	2	2.21
50	1.8	2.2, 4.2, 6.2, 8.2, 10.2	3	1.71
50	1.8	2.2, 4.2, 6.2, 8.2, 10.2	4	1.71

Table 1. Geometric variables D, r, d and h (figure 1b) and impact speed U of surface-patterned disks.

disk are shown in figure 2. Here, a 5 mm-thick flat disk of diameter $D = 50$ mm was used. For the surface-patterned disk, a 2 mm-thick perforated disk ($r = 1.8$ mm and $d = 4.2$ mm) with the same D was attached to the flat disk, giving the total thickness of 7 mm. They were dropped from a height of $H = 15$ cm, resulting in an impact speed of $U = 1.71$ m s^{-1}. Compared with the weight of the entire falling unit, the difference in weight between the flat disk and the surface-patterned disk is negligible, and thus it is assumed that the falling units have the same momentum. Here, $t = 0$ is designated as the instant of free-surface impact, and the time at which the maximum impact force F_{max} occurs is denoted by t_{peak}. The flat disk experiences $F_{max} = 193.8$ N at $t_{peak} = 0.575$ ms, while the surface-patterned disk yields $F_{max} = 92.1$ N at $t_{peak} = 0.750$ ms (figure 2). The F_{max} value of the surface-patterned disk is less than half that of the flat disk, and the peak appears at a later time. That is, the surface pattern notably reduces the maximum impact force. Although these two disks have different thicknesses, the comparison of the maximum impact forces is not affected by the disk thickness. We confirmed that the maximum impact force for the flat disk did not change when its thickness was increased to 7 mm. Furthermore, the acrylic disk of thickness 5 mm was rigid enough to avoid elastic deformation affecting the maximum impact force.

After the peak, the force profile shows fluctuations for both the flat and surface-patterned disks (figure 2). Owing to the limitations of our experimental set-up, the force sensor picks up oscillations in the rod arising from the impulsive load. That is, the fluctuations do not originate from flow phenomena such as hydrodynamic loading as a result of reflected shock waves. Residual oscillations after the peak impact force were also reported by Vincent *et al.* (2018), who measured the impact forces on wedges and noted that oscillations were due to the drop mechanism of the model. Because the initial peak of the impact force is our primary interest, subsequent fluctuations after the initial peak are not considered in the analysis of the magnitude and duration of the impact force.

The impact force was measured five times for each surface-patterned disk, and the average of the maximum impact force is presented in figure 3. In figure 3(a), the value of F_{max} decreases with d for the same r (the same colour in figure 3a), with $D = 50$ mm, $h = 2$ mm and $U = 1.71$ m s^{-1} kept constant. The total area of the holes in the surface pattern, A_{hole}, becomes larger as the side length d of the holes increases, and the increase in A_{hole} reduces the maximum impact force F_{max}. Furthermore, the F_{max} values for different surface-patterned disks are similar as long as they have similar A_{hole}, despite different

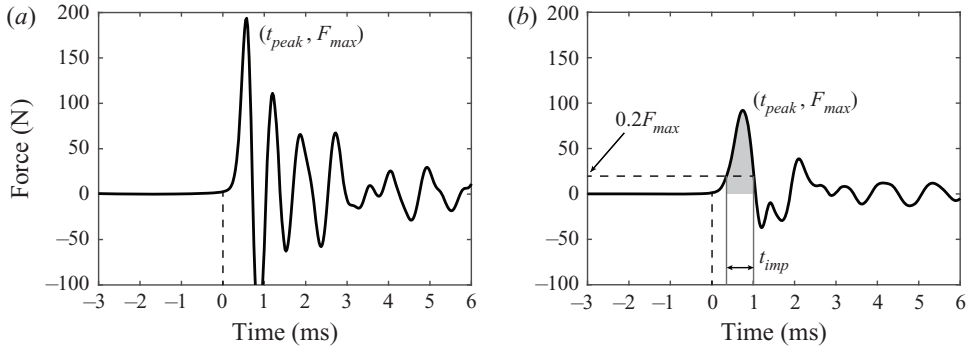

Figure 2. General impact force profiles for (*a*) a flat disk ($D = 50$ mm) and (*b*) a surface-patterned disk ($D = 50$ mm, $r = 1.8$ mm, $d = 4.2$ mm, $h = 2$ mm) impacting a free surface at $U = 1.71$ m s^{-1}. The impact duration t_{imp} is defined as the time interval during which the impact force exceeds $0.2F_{max}$ and is discussed in § 3.4. High-speed images for the water entry of the two disks are provided in the supplementary movie 1 available at https://doi.org/10.1017/jfm.2021.123.

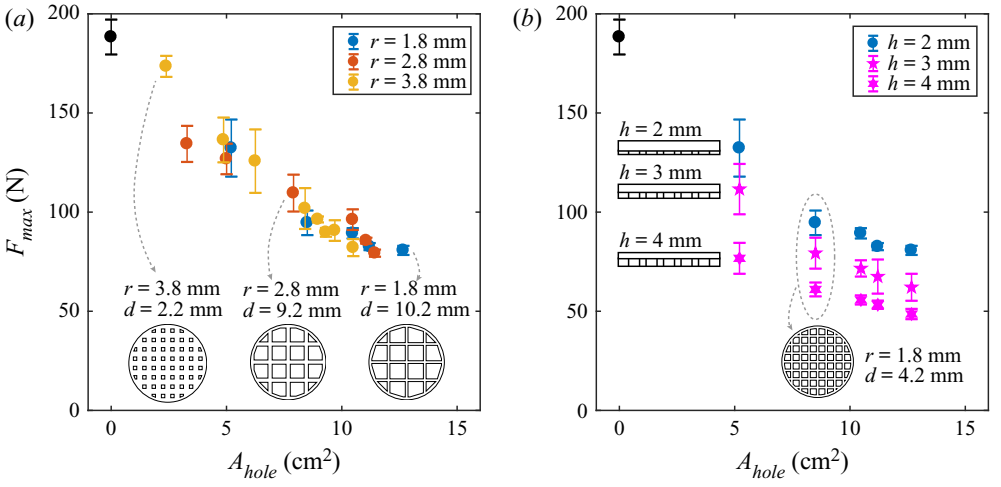

Figure 3. Maximum impact force F_{max} for different surface-patterned disks with $D = 50$ mm at $U = 1.71$ m s^{-1} as a function of A_{hole}. Here F_{max} for a 5 mm-thick flat disk is located at $A_{hole} = 0$ in black solid circles (•). (*a*) Cases with the same r are shown in the same colour; $h = 2$ mm in all cases. (*b*) Cases with the same h have the same shape: circles, $h = 2$ mm; five-pointed stars, 3 mm; six-pointed stars, 4 mm. For detailed information on the dimensions, see table 1.

pattern details. In other words, the maximum impact force seems to be determined by the total area of the holes, regardless of the shape of the pattern. Here, the flat disk is considered as a disk with no holes, $A_{hole} = 0$ (see the black solid circle in figure 3). Compared with F_{max} for the flat disk, which is 188.3 N, the surface-patterned disks have F_{max} values that could be as low as 79.3 N (a 58 % reduction) (figure 3*a*). The attachment of a surface pattern to a flat disk consistently reduces the maximum impact force, and the magnitude of this reduction becomes greater with increasing A_{hole}.

Additional experiments were conducted by changing the hole depth h for a given A_{hole} to clarify whether the reduction in F_{max} is simply due to a decrease in the area that is in contact with the free surface, $A_{pattern}$ (grey area in figure 1*b*, $(\pi D^2)/4 = A_{pattern} + A_{hole}$), or is caused by some complex flow phenomena that are induced by the holes. Although the

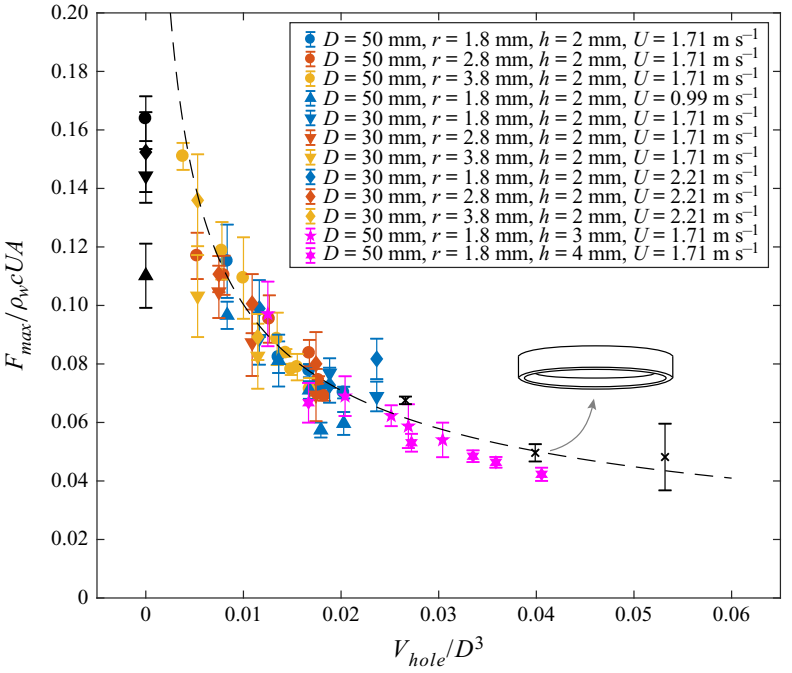

Figure 4. Coefficient of maximum impact force, $F_{max}/\rho_w cUA$, versus dimensionless total volume of holes, V_{hole}/D^3. The extreme case with the maximum hole volume is denoted by the black cross symbol (×) for each of $h = 2$, 3 and 4 mm; the disk image in the figure is for $h = 3$ mm. The cases of a 5 mm-thick flat disk, shown in black, are located at $V_{hole}/D^3 = 0$. The dashed line is a theoretical prediction from (3.14) derived in § 3.3 for the surface-patterned disks.

surface-patterned disks have the same d and r (and thus the same A_{hole}), F_{max} decreases with the increase in h (figure 3*b*). A reduction in the maximum impact force of up to 42 % is achieved as h increases from 2 to 4 mm for the same surface pattern (and the same A_{hole}). In other words, figure 3 demonstrates that both A_{hole} and h are important geometric parameters of the surface-patterned disks that determine F_{max}.

To address the combined effect of A_{hole} and h, the maximum impact forces are plotted versus V_{hole}/D^3 for various surface-patterned disks, where $V_{hole}(= A_{hole}h)$ is the total volume of the holes created by the surface pattern (figure 4). Here, the coefficient of maximum impact force is introduced as $F_{max}/\rho_w cUA$, where $\rho_w = 998$ kg m^{-3} is the density of water, $c = 343$ m s^{-1} is the speed of sound in air, U is the impact speed and $A = (\pi D^2)/4$ is the frontal area of the disk. This non-dimensionalization comes from the theoretical approach for the free-surface impact of a flat-bottomed body. To predict the slamming pressure of a flat plate, von Kármán (1929) used momentum conservation to suggest that $p_{max} = \rho_w c_w U$, in which the pressure rise propagates at the speed of sound in water, c_w. In a later study, Verhagen (1967) considered the effect of a thin layer of air trapped between the flat plate and the free surface at the moment of impact, and modified the relation to $p_{max} \sim \rho_w cU$, where c is the speed of sound in air. In figure 4, the maximum impact force coefficients $F_{max}/\rho_w cUA$ collapse onto a single monotonically decreasing curve with respect to the dimensionless total volume of the holes, V_{hole}/D^3.

Let us consider the case of an extremely large hole. For special cases where d is very close to D, only a 2 mm rim remains with a single large hole inside, giving the maximum hole volume for given disk diameter D and hole depth h; e.g. the disk in the inset of

figure 4. For each of $h = 2$, 3 and 4 mm ($D = 50$ mm, $U = 1.71\ \mathrm{m\,s^{-1}}$), the case with the maximum hole volume corresponds to each of the three black cross symbols located in $0.02 < V_{hole}/D^3 < 0.06$ (figure 4). The values of $F_{max}/\rho_w cUA$ in these extreme cases follow the same trend as those for the mesh-like surface-patterned disks. Note that the disk with the maximum value of V_{hole}/D^3 for given values of D and h has a flat surface inside the rim, and the only difference from the flat disk with $V_{hole}/D^3 = 0$ is the existence of the rim. Interestingly, despite this similarity in shape, the values of $F_{max}/\rho_w cUA$ are much smaller than those of the flat disks; compare two groups of data coloured black between $V_{hole}/D^3 = 0$ (flat disk) and $0.02 < V_{hole}/D^3 < 0.06$ (disk with the maximum hole volume) in figure 4.

Figure 4 reveals that, regardless of the shape of the pattern, the total volume of the holes created by the surface pattern, V_{hole}/D^3, characterizes the reduction in maximum impact force, $F_{max}/\rho_w cUA$, in the case of a surface-patterned disk. To support this argument, we tested other regular and irregular surface patterns and obtained consistent experimental results; see the Appendix. In addition to the experimental measurements, the trend in figure 4 will be established by theoretical analysis in § 3.3.

3.2. *Air entrapment*

In this section, based on flow visualization, we present a qualitative explanation of why the maximum impact force on a surface-patterned disk decreases as the total volume of holes in the surface pattern increases. The air bubbles trapped inside the holes at the beginning of the impact process are mainly responsible for this result. From the visualization of the bottom and side of a disk impacting a free surface, we can observe the trapping of air inside the holes and identify the subsequent complex behaviour of the air bubbles (figure 5 and supplementary movies 2 and 3). After the moment of impact, the trapped air becomes visible as it escapes from the holes (figures 5*a*iii,*a*iv and 5*b*ii,*b*iii). As the disk descends farther inside the water, vented air bubbles remain beneath the disk, moving radially towards the edge of the disk. From the side view, the radial motion of the bubbles is clear; a bubble inside the red circle is tracked and observed to move to the edge of the disk in figure 5(*b*iv–*b*vi). When the bubble reaches the edge of the disk, it joins the air cavity that begins at the disk edge and forms behind the disk; the bubble inside the blue circle in figure 5(*b*iv,*b*v) disappears in figure 5(*b*vi).

For the correlation between the generation of impact force and the motion of trapped air bubbles during the initial impact phase, the force profile is analysed in accordance with the corresponding images of a surface-patterned disk (figure 6*a*). At the instant of impact (figure 6*a*i) and during the steep rise in the impact force (figure 6*a*ii,*a*iii), air is compressed inside the holes. As the impact force reaches its maximum and begins to diminish, air bubbles start to escape from the edges of each hole (figure 6*a*iv). Thereafter, the bubbles continue to be vented from the holes (figure 6*a*v,*a*vi).

To elucidate the dynamics of the air bubbles inside the holes, an advanced optical set-up is required for the clear visualization of the bubbles. Alternatively, in this study, we conjecture the characteristic motion of the trapped air bubbles (figure 6*b*) based on our experimental observations (bottom view) and the results of previous studies. As the disk continues to descend through the water immediately after the impact (figure 6*b*i), the patterned part (grey colour in figure 6*b*) acts locally as a flat plate of width r. It is well known that the pinning of a contact line is universally observed during cavity formation behind an impacting body (Truscott *et al.* 2014). Similar to the initial stage of air-cavity and splash formation in the impact of a flat plate (Mayer & Krechetnikov 2018), the pinning of the contact line at the corner of the pattern occurs upon impact, as shown

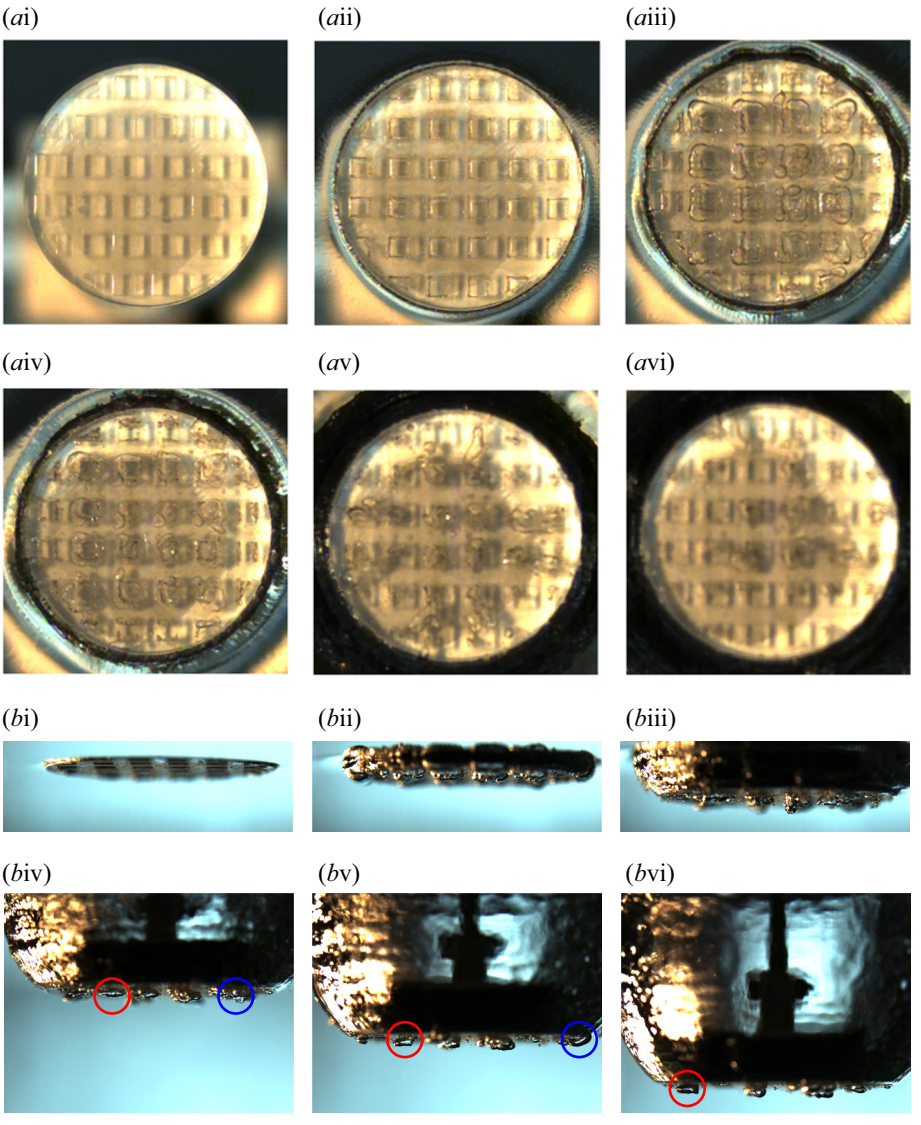

Figure 5. Visualization of air bubbles beneath a surface-patterned disk upon water entry in (*a*) bottom view and (*b*) side view: $D = 50$ mm, $r = 3.8$ mm, $d = 4.2$ mm, $h = 2$ mm, and $U = 1.71$ m s^{-1}. In the bottom view, the focal plane of the images is set near the free surface. Thus, in panels (*a*v, *a*vi), the images become blurred after the disk has passed the focal plane. See supplementary movies 2 and 3. The times are (*a*i) $t = 0.00$ ms, (*a*ii) $t = 0.45$ ms, (*a*iii) $t = 1.15$ ms, (*a*iv) $t = 1.80$ ms, (*a*v) $t = 11.90$ ms, (*a*vi) $t = 19.65$ ms, (*b*i) $t = 0.35$ ms, (*b*ii) $t = 1.25$ ms, (*b*iii) $t = 4.00$ ms, (*b*iv) $t = 9.25$ ms, (*b*v) $t = 15.00$ ms, (*b*vi) $t = 20.60$ ms.

in figure 6(*b*ii,*b*iii). Simultaneously, the water displaced by the patterned part moves into the hole, and therefore the air inside the hole becomes compressed. When the air pressure inside the hole reaches a certain value, the pressurized air penetrates the contact line at the corner of the pattern (figure 6*b*iv). Afterwards, the air is depressurized and flows out of the gaps at the edge of the holes (figure 6*b*v), as observed in the bottom view (figure 6*a*). Once a significant volume of the trapped air has escaped from the hole, the hole is filled with water (figure 6*b*vi).

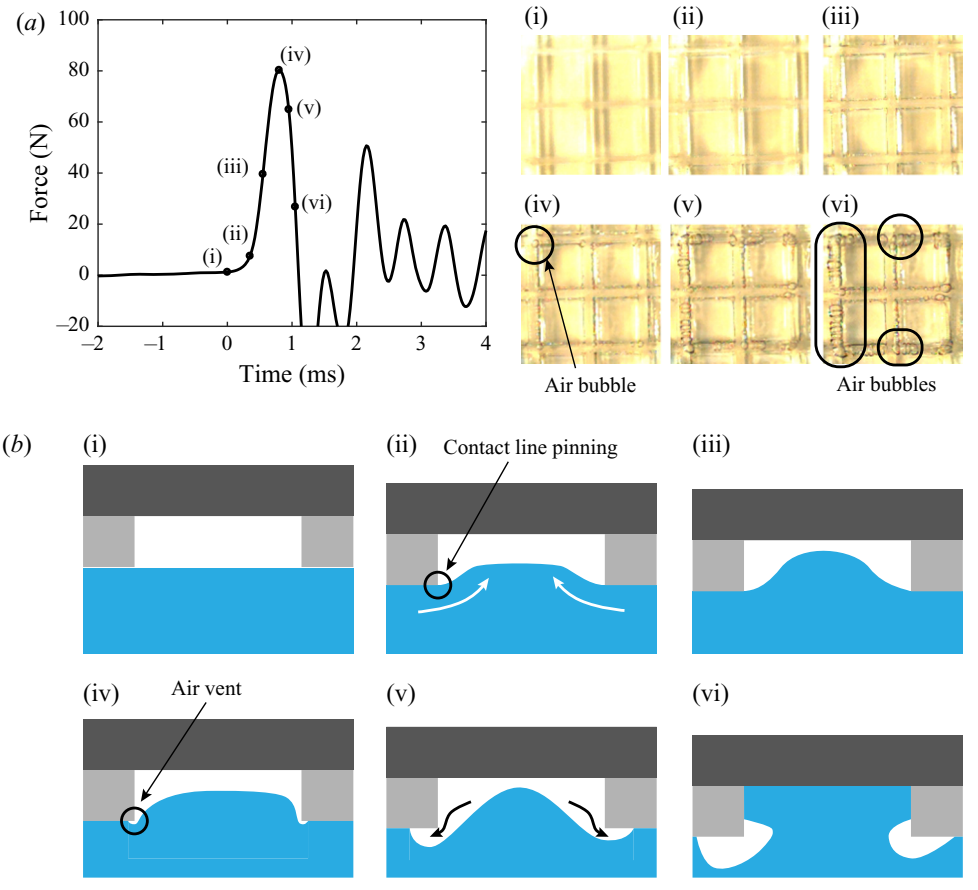

Figure 6. (*a*) Profile of impact force for a surface-patterned disk ($D = 50$ mm, $r = 1.8$ mm, $d = 10.2$ mm, $h = 2$ mm and $U = 1.71$ m s^{-1}) and corresponding images of the bottom surface focusing on four holes at the disk centre (bottom view). (*b*) Schematic diagrams of the dynamics of air bubbles inside the holes. The grey block and the white area denote a surface pattern and a single hole, respectively. Subpanels (i–vi) in panel (*a*) correspond to subpanels (i–vi) in panel (*b*). See supplementary movie 4 for panel (*a*).

When the air bubble penetrates the contact line and vents out of the hole, it mostly escapes through the side that is farther from the centre of the disk, as demonstrated in figure 6(*a*iv–*a*vi) (magnified views of the four holes at the disk centre). For a flat disk, the pressure at the centre of the surface is greater than that at the edge (Okada & Sumi 2000; Ma *et al.* 2016). Similarly, for our model, we may assume that the pressure on the surface is not uniform, but decreases radially from its centre. Thus, as the pressurized air overcomes the water pressure inside the hole, the air bubble starts to vent through the side farther from the centre, where the pressure is lower.

The characteristic behaviour of trapped air bubbles in a surface-patterned disk (figures 5 and 6) differs notably from that of a flat-bottomed structure. It is well known that, when a flat-bottomed structure impacts a free surface, a thin layer of air becomes trapped and is broadly distributed. Verhagen (1967) confirmed this trapping of a thin layer of air below a flat plate using high-speed images, and considered the compressibility of air to explain the peak pressure exerted on the plate. The behaviour of the trapped layer of air beneath the flat plate was clearly visualized, with initial touchdown at the edge and collapse of air from the edge to the centreline (see Mayer & Krechetnikov (2018), figure 24). Similar dynamics

were also observed for a flat disk in which the trapped air layer had a circular shape and collapsed toward the centre of the disk (see Ermanyuk & Gavrilov (2011), figure 4).

The impact force exerted on a surface-patterned disk is the spatial integral of pressure over the entire frontal area of the disk. This frontal area of the disk can be decomposed into $A_{pattern}$ and A_{hole} (figure 1*b*). The pressure over A_{hole} compresses the trapped air, imposing a pressure on the disk until the air eventually vents out at some point during the impact process. The compression of air contributes to a reduction in peak pressure, and therefore disks with a greater A_{hole} (and V_{hole}) generally yield a reduced peak force for the same model conditions (figures 3 and 4). The role of confined air in reducing the peak pressure was also described by Mathai *et al.* (2015), who found that a concave-nosed body exhibited a smaller peak pressure than a flat or convex-nosed body because of the presence of trapped air. In summary, our systematic experimentation has revealed that the compression and depressurization of trapped air bubbles during the initial impact phase leads to the rise and fall of the impact force and accounts for a reduction in the peak impact force.

3.3. *Theoretical prediction of impact force*

Although the previous sections described the effects of a surface pattern and trapped air inside the holes based on force measurements and flow visualization, theoretical analysis is also necessary to provide quantitative predictions of how the impact force is affected by the volume of holes on a surface-patterned disk. Previous studies on the water impact of a flat-bottomed body addressed the preimpact deformation of the free surface by the approaching body (Verhagen 1967; Ermanyuk & Ohkusu 2005; Mayer & Krechetnikov 2018). The deformation of the free surface enables the entrapment of a thin, but widespread, air layer at the instant of impact, producing the air-cushioning effect. However, in our analysis of a surface-patterned disk, the preimpact deformation of the free surface is assumed to be negligible because of its minor magnitude; the volume of the entrapped air layer between the disk bottom surface and the free surface is so small compared with the total volume of the holes. That is, the free surface is assumed to be flat before the impact.

When the surface-patterned disk impacts the free surface, air is trapped inside the holes (figure 6). The impact force experienced by the surface-patterned disk is the spatial integral of the pressure of the water that the disk contacts as well as that of the trapped air inside the holes. Let p_{hole} be the pressure on the holes, $p_{pattern}$ be the pressure on the pattern surface and p_0 be the atmospheric pressure. Then, the upward force F exerted on the disk is

$$F = \int p_{hole}\,\mathrm{d}A_{hole} + \int p_{pattern}\,\mathrm{d}A_{pattern} - p_0 A = \bar{p}_{hole}A_{hole} + \bar{p}_{pattern}A_{pattern} - p_0 A, \tag{3.1}$$

where $\bar{p}_{hole}$ and $\bar{p}_{pattern}$ denote the mean pressure over the surface area for the holes and the patterned part, respectively. Here, we assume that the air pressure is uniform inside each hole and the water pressure on the patterned surface changes linearly between two nearby holes. Accordingly, the relation between $\bar{p}_{hole}$ and $\bar{p}_{pattern}$ is given as $\bar{p}_{pattern} = \bar{p}_{hole} = \bar{p}$, and the upward force F reduces to

$$F = (\bar{p} - p_0)A. \tag{3.2}$$

After the instant of impact, water enters the hole and compresses the trapped air. Although the trapped bubbles exhibit complex behaviour, we simplify the decrease in

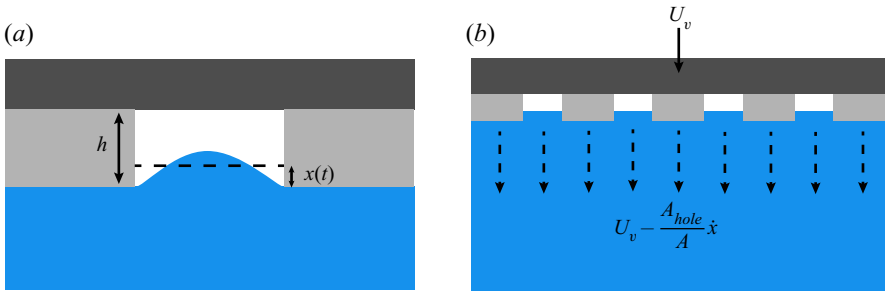

Figure 7. Schematic diagram after impact. (*a*) After the impact, air is trapped and compressed inside the hole. The mean depth of water penetration inside the hole is denoted as $x(t)$. (*b*) Added mass of the disk is pushed downward with an effective speed of $U_{eff} (= U_v - A_{hole}\dot{x}/A)$.

volume of the trapped air at each hole as an increase in the mean water penetration $x(t)$ with respect to the bottom surface of the pattern (figure 7*a*) and assume that $x(t)$ is uniform in all holes of the disk. Without a surface pattern, water on the disk–water interface accelerates to a downward speed of U_v, the same as the speed of the disk, soon after the impact. However, for a surface-patterned disk, some portion of the water moves upward into the holes through A_{hole} at a speed of $\dot{x}(t)$ relative to the disk. That is, the interface in contact with the surface pattern moves downward with a speed of U_v, and the interface in contact with air in the holes moves downward with a speed of $U_v - \dot{x}$. The spatially averaged effective speed U_{eff} of the water on the interface is then

$$U_{eff} = \frac{[(A - A_{hole})U_v + A_{hole}(U_v - \dot{x})]}{A} = U_v - \frac{A_{hole}}{A}\dot{x}. \tag{3.3}$$

In other words, in comparison with the speed of the disk U_v, the effective (net) downward speed of water on the free surface is $U_v - A_{hole}\dot{x}/A$ due to the existence of the holes (figure 7*b*).

The peak impact force is generally explained in terms of the added mass of water that is accelerated by a solid object. The added mass of a flat disk upon water entry is expressed as $(\rho_w D^3)/6$ (Glasheen & McMahon 1996*b*). In this study, however, the presence of the surface pattern may alter the fluid behaviour beneath the disk, as discussed in § 3.2. Therefore, we express the added mass of the surface-patterned disk as $k\rho_w D^3$, where the unknown constant k will be assigned later. With (3.2), the equation of motion for the added mass becomes

$$(\bar{p} - p_0)A = k\rho_w D^3 \frac{\mathrm{d}}{\mathrm{d}t}\left(U_v - \frac{A_{hole}}{A}\dot{x}\right) = -k\rho_w D^3 \frac{A_{hole}}{A}\ddot{x}. \tag{3.4}$$

Because the falling unit is heavy and the phase for the first peak of the impact force is very short, typically $O(1$ ms) (figure 2*b*), the impact speed U_v of the disk is assumed to be constant as U during the impact phase: $\mathrm{d}U_v/\mathrm{d}t = \mathrm{d}U/\mathrm{d}t = 0$. The initial conditions are $x(0) = 0$ and $\dot{x}(0) = UA/A_{hole}$ because the water initially has zero speed: $U - A_{hole}\dot{x}(0)/A = 0$.

According to Verhagen (1967), air entrapped between a falling plate and a deformed free surface becomes compressed even before impact. Although we neglected the free surface deformation before the impact, air inside the holes may be compressed before the impact. Let a new variable $\bar{p}_c$ denote the pressure of air inside the holes right at the moment of impact. Because the air inside the holes is compressed very quickly as water

penetrates, from $\bar{p}_c$ to $\bar{p}$ in (3.4), the adiabatic relation $\bar{p}_c h^\gamma = \bar{p}(h-x)^\gamma$ holds. Then, $\bar{p} = \bar{p}_c(1-x/h)^{-\gamma} \approx \bar{p}_c(1+\gamma x/h)$, and (3.4) becomes

$$(\bar{p}_c - p_0) + \frac{\gamma \bar{p}_c}{h}x + \frac{k\rho_w D^3}{A}\frac{A_{hole}}{A}\ddot{x} = 0. \tag{3.5}$$

Solving (3.5) with the initial conditions, we obtain

$$x(t) = -\frac{\bar{p}_c - p_0}{\gamma \bar{p}_c/h} + \frac{\bar{p}_c - p_0}{\gamma \bar{p}_c/h}\cos(\omega t) + \frac{A}{A_{hole}}\frac{U}{\omega}\sin(\omega t), \tag{3.6a}$$

$$\dot{x}(t) = -\frac{\bar{p}_c - p_0}{\gamma \bar{p}_c/h}\omega \sin(\omega t) + \frac{A}{A_{hole}}U\cos(\omega t), \tag{3.6b}$$

where

$$\omega = \left(\frac{\gamma \bar{p}_c/h}{(k\rho_w D^3/A)(A_{hole}/A)}\right)^{1/2}. \tag{3.7}$$

Substituting (3.6*a*) into (3.4), the impact force F is

$$F(t) = k\rho_w D^3 \frac{A_{hole}}{A}\left(\frac{\bar{p}_c - p_0}{\gamma \bar{p}_c/h}\omega^2 \cos\omega t + \frac{A}{A_{hole}}U\omega \sin\omega t\right). \tag{3.8}$$

To determine the added-mass coefficient k, the impulse I imposed on the surface-patterned disk is computed by integrating $F(t)$ over impact duration, $t = 0$–T:

$$I = \int_0^T F\,\mathrm{d}t = k\rho_w D^3 \frac{A_{hole}}{A}\left(\frac{\bar{p}_c - p_0}{\gamma \bar{p}_c/h}\omega \sin\omega T + \frac{A}{A_{hole}}U(1-\cos\omega T)\right). \tag{3.9}$$

As will be discussed in § 3.4, this impulse should be equal to that imposed on a flat disk at the instant of impact ($I_{flat} = (\rho_w D^3 U)/6$). Because the impulse should be independent of T and the time history of the impact force during impulse duration looks like the first half-period of a harmonic function according to our experiment (figure 2*b*), $T = \pi/\omega$ is a likely theoretical prediction of the impulse duration. The impulse I is then given by

$$I = \int_0^{\pi/\omega} F\,\mathrm{d}t = 2k\rho_w D^3 U, \tag{3.10}$$

which results in $k = 1/12$; I should be equal to I_{flat} $(= (\rho_w D^3 U)/6)$.

When seen by an observer fixed on the ground, the free surface, which is initially in a stationary state, is accelerated by the disk to an effective downward speed of $2U(= U - A_{hole}\dot{x}(\pi/\omega)/A)$ at $t = T(= \pi/\omega)$. When seen by an observer riding on the disk, the free surface approaches the observer with a speed of U at $t = 0$ and moves away from the observer with a speed of U at $t = T(= \pi/\omega)$. In this sense, the role of the air bubbles inside the holes may be described as a spring. Before impact, the spring (air bubble inside a hole) absorbs a loading by an object (water) with an incoming speed U relative to the spring, and at the end of the impact phase the object (water) moves in the opposite direction with a speed U relative to the spring. Because the speed of the disk is U in the ground reference, the effective downward speed U_{eff} of the water eventually should become $2U$ in the ground reference. Thus, the equivalence of impulse between the flat disk and the surface-patterned disk implies that the added mass $(\rho_w D^3)/12$ of the surface-patterned disk is half that of the flat disk with no surface pattern, $(\rho_w D^3)/6$.

According to (3.8) and the relation between F and T such that $F(T) = F(\pi/\omega) = 0$, $\bar{p}_c$ should be equal to p_0. This relation can also be obtained using our experimental data

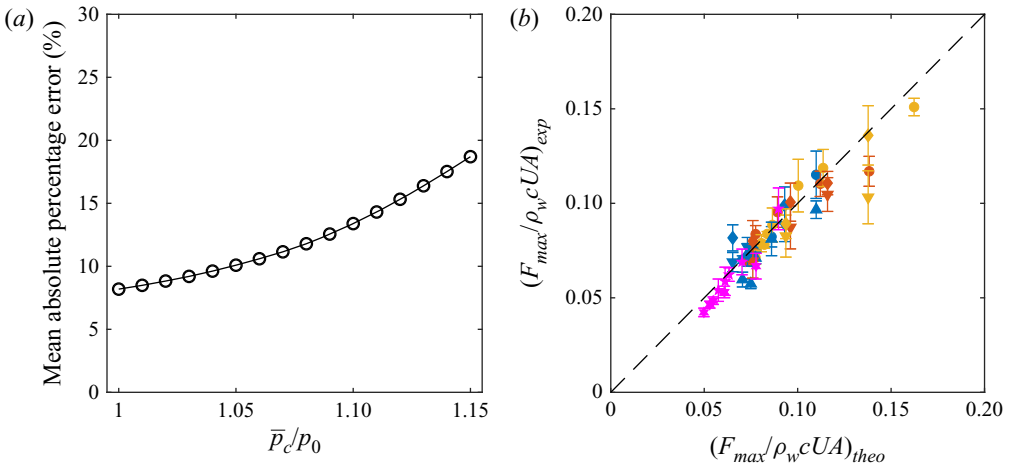

Figure 8. (*a*) Mean absolute percentage error between experimental and theoretical values of the maximum impact force F_{max} as a function of $\bar{p}_c/p_0$. (*b*) Comparison between experimental and theoretical values of the maximum impact force coefficient $F_{max}/\rho_w cUA$ for $\bar{p}_c/p_0 = 1$.

for maximum impact force. The maximum impact force corresponds to the maximum amplitude of the solution in (3.8), and the maximum impact force coefficient $F_{max}/\rho_w cUA$ is expressed as

$$\frac{F_{max}}{\rho_w cUA} = \left[\left(\frac{\bar{p}_c - p_0}{\rho_w cU}\right)^2 + \frac{\gamma \bar{p}_c}{12\rho_w c^2}\frac{D^3}{V_{hole}}\right]^{1/2}. \tag{3.11}$$

To determine $\bar{p}_c$ from our experimental data, the mean absolute percentage error is evaluated for a given $\bar{p}_c$ (figure 8*a*), which is defined as $\Sigma_{i=1}^{n}|(F_{max,exp,i} - F_{max,theo,i})/F_{max,exp,i}|/n$, where n is the total number of experimental cases and $F_{max,exp,i}$ and $F_{max,theo,i}$ are the experimental and theoretical values, respectively, of the maximum impact force for each case i. In figure 8(*a*), the mean absolute percentage error is smallest at $\bar{p}_c/p_0 = 1$, which indicates that (3.11) is best fitted with our experimental data when $\bar{p}_c = p_0$ (figure 8*b*).

Interestingly, the relation $\bar{p}_c = p_0$ shows that the air inside the gap between the free surface and the surface-patterned disk is not compressed, and maintains the atmospheric pressure before impact, unlike for the flat disk with no pattern. For the flat-disk case, the air in the gap begins to be compressed when the radial velocity at the rim of the disk is equal to the speed of sound before impact. Thus, the air pressure at the instant of impact increases significantly beyond p_0 (Verhagen 1967). However, for the surface-patterned disk, the holes inside the surface pattern buffer the pressure increase of air between the disk and the free surface. The pressure inside the gap changes little before impact and can be approximated as p_0. Note that $\bar{p}_c = p_0$ means the air remains uncompressed before impact and does not contradict our previous argument that the air becomes compressed like a spring after impact.

With $\bar{p}_c = p_0$, (3.6*a*), (3.8) and (3.11) are simplified as follows:

$$x(t) = \frac{A}{A_{hole}}\frac{U}{\omega}\sin(\omega t), \tag{3.12}$$

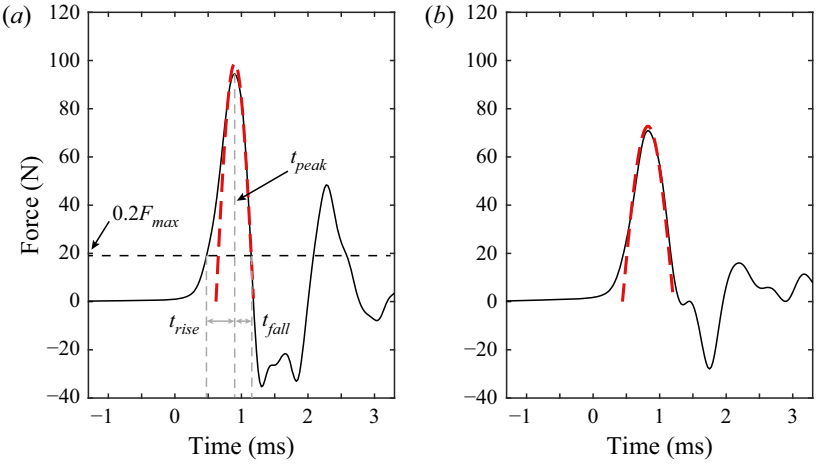

Figure 9. Time history of the impact force for a surface-patterned disk: (*a*) $V_{hole}/D^3 = 0.014$ ($D = 50$ mm, $r = 1.8$ mm, $d = 4.2$ mm, $h = 2$ mm and $U = 1.71\ \mathrm{m\,s^{-1}}$); (*b*) $V_{hole}/D^3 = 0.025$ ($D = 50$ mm, $r = 1.8$ mm, $d = 6.2$ mm, $h = 3$ mm and $U = 1.71\ \mathrm{m\,s^{-1}}$). The red dashed line is given by (3.13) with a phase shift that matches the phase of the peak.

$$F(t) = \frac{1}{12}\rho_w D^3 U\omega \sin \omega t, \tag{3.13}$$

$$\frac{F_{max}}{\rho_w cUA} = \left(\frac{\gamma p_0}{12\rho_w c^2}\right)^{1/2} \left(\frac{V_{hole}}{D^3}\right)^{-1/2}. \tag{3.14}$$

Although (3.12) and (3.13) are expressed in the form of an oscillation, the equations are only physically meaningful until the penetration height x returns to zero at $t = T(= \pi/\omega)$. After $t = T$, x is negative in (3.12), which means that the air has escaped from the holes, and our analysis becomes invalid.

The time history of the impact force acting on the disk is compared between the theoretical prediction (3.13) and the experimental measurement for two different cases (figure 9). For comparison, the peak of the theoretical curve is positioned at the same x value (time) as that of the experimental curve. The theoretical prediction matches well with the experimental data if arbitrary phase shift is applied to the theoretical curve of (3.13). The phase shift is necessary because the rise in the experimental impact force is more gradual and lasts longer. The theoretical profile is symmetric with respect to its peak, whereas the profile obtained experimentally is asymmetric. Our theoretical approach might not capture important interface dynamics that determine the impact force at the early rise phase of the impact force. Future research should examine exactly how trapped air bubbles behave in the holes of a surface pattern and improve the current theoretical model to account for the asymmetric time history of the impact force. Furthermore, the maximum impact force coefficient (3.14) provides the dashed line in figure 4. Although we made several assumptions to simplify the problem, (3.14) is in good agreement with most of the experimental data for surface-patterned disks.

3.4. *Impact duration and impulse*

We now consider the impact duration and impulse to examine the water impact of a surface-patterned disk from the perspective of momentum transfer. In the experimental results, the impact duration t_{imp} is defined as the time during which the impact force

exceeds $0.2F_{max}$ before and after its peak (figure 2*b*), and the impulse I is calculated by integrating the impact force over the impact duration (see the shaded area in figure 2*b*). Because it was difficult to determine, with the necessary accuracy, the time at which the impact force becomes non-zero from the experimental results, a threshold was adopted to obtain the impact duration, and this was varied to find an appropriate value. The computed impulse was similar when the threshold value was between $0.1F_{max}$ and $0.3F_{max}$, but decreased sharply beyond $0.4F_{max}$. The main arguments in this section are not affected when the threshold is between $0.1F_{max}$ and $0.3F_{max}$, and so $0.2F_{max}$ was chosen to define t_{imp}. Because of the difficulty in specifying an exact contact time in water impact problems, previous studies on the water entry of solid objects have tended to compute the impulse exerted on the objects using different time ranges (Huera-Huarte, Jeon & Gharib 2011; Ma *et al.* 2016; Speirs *et al.* 2019). In that the impulse refers to momentum loss by water impact, the dimensionless impulse is obtained by dividing the impulse by the momentum of the falling unit at impact, MU. Here M is the total mass of the falling unit (dashed box in figure 1*a*), and this is set to be $M = 1.3$ kg, regardless of which surface-patterned disk is used, because each disk accounts for less than 2 % of the mass of the falling unit.

In contrast to $F_{max}/\rho_w cUA$ (figure 4), the dimensionless impulse I/MU is not strongly affected by V_{hole}/D^3 (figure 10*a*). That is, while the size of the disk is critical for the impulse, the shape of the surface pattern itself has no significant effect. For surface-patterned disks with $D = 50$ mm, the values of I/MU are mostly within a narrow range between 0.015 and 0.021, regardless of the shape of the surface pattern and the depth of the holes. Moreover, surface-patterned disks with $D = 30$ mm undergo much smaller momentum loss than those with $D = 50$ mm, and exhibit an almost constant $I/MU \approx 0.005$. Note that I/MU for the flat disk ($V_{hole}/D^3 = 0$) is also within the range of the surface-patterned disks in figure 10(*a*), which validates our approach using $I = I_{flat}$ to determine the added-mass coefficient k in § 3.3. The value of I/MU depends on the disk diameter D rather than V_{hole}/D^3. For a disk with larger D, a greater volume of water per unit disk area is displaced and accelerated by the impact, leading to an increase in the momentum loss. A similar result was reported by Glasheen & McMahon (1996*b*). Note that the impulses in the present study ($0.0098\ \mathrm{N\,s} \leq I \leq 0.045\ \mathrm{N\,s}$) lie in the same range as the results of Glasheen & McMahon (1996*b*), who used flat disks with diameters between 25.4 and 61.4 mm and impact velocities from 0.562 to 3.11 $\mathrm{m\,s^{-1}}$, which cover the ranges of D and U in our experimental models (table 1).

The impact duration t_{imp} defined above for the experimental results corresponds to $T = \pi/\omega$ theoretically, according to our analysis in § 3.3: $F(0) = F(\pi/\omega) = 0$ from (3.13). The impulse during the period $t = 0$–π/ω is $I = (\rho_w D^3 U)/6$ in (3.10). The corresponding dimensionless impulse $I/MU(= \rho_w D^3/6M)$ is approximately 0.016 and 0.003 for $D = 50$ mm and 30 mm, respectively, which slightly underestimate the experimental measurements (figure 10*a*). Nevertheless, (3.10) can capture the aforementioned trend based on our experimental results: $I/MU(= \rho_w D^3/6M)$ is independent of A_{hole} and V_{hole}, but is affected by D for a given mass of the falling unit.

From (3.13), the maximum impact force coefficient is expressed in terms of the impact duration $t_{imp}(\approx T = \pi/\omega)$ as

$$\frac{F_{max}}{\rho_w cUA} = \frac{1}{3}\left(\frac{t_{imp}}{D/c}\right)^{-1}. \tag{3.15}$$

For the same impulse (same D and U), the maximum impact force is inversely proportional to the impact duration. As predicted by (3.15), for our experimental data, $F_{max}/\rho_w cUA$ depends solely on the dimensionless impact duration $t_{imp}/(D/c)$, and seemingly collapses

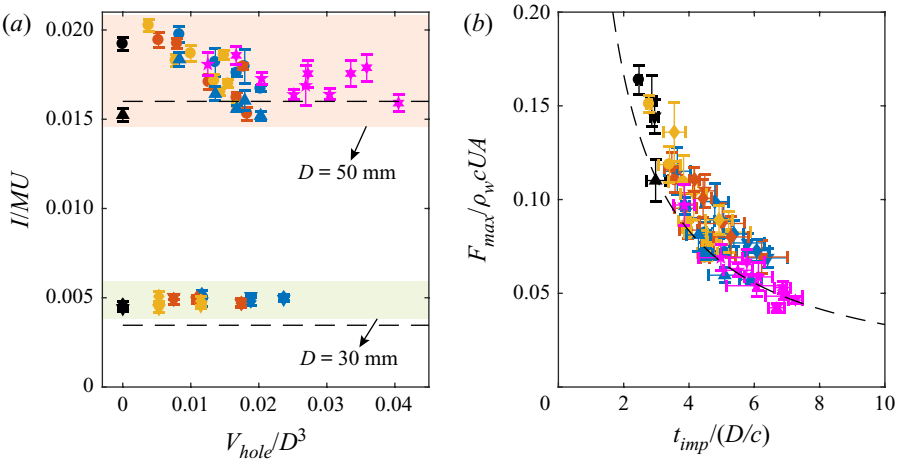

Figure 10. (*a*) Dimensionless impulse I/MU versus V_{hole}/D^3 for two different disk diameters, $D = 50$ mm and 30 mm. (*b*) Maximum impact force coefficient $F_{max}/\rho_w cUA$ versus dimensionless impact duration $t_{imp}/(D/c)$. In panels (*a*,*b*), the dashed line shows the theoretical prediction, $I/MU = \rho_w D^3/6M$ and (3.15). The notation of the symbols is the same as in figure 4.

onto a single curve of (3.15) for all surface patterns (d, r and h), disk diameters D and impact velocities U considered in this study (figure 10*b*). That is, the application of a surface pattern to the disk can reduce $F_{max}/\rho_w cUA$ by increasing $t_{imp}/(D/c)$.

In figures 4 and 10(*b*), we find that $F_{max}/\rho_w cUA$ decreases inversely with V_{hole}/D^3 and $t_{imp}/(D/c)$, respectively. From (3.14) and (3.15),

$$\frac{t_{imp}}{D/c} = \left(\frac{4\rho_w c^2}{3\gamma p_0}\right)^{1/2} \left(\frac{V_{hole}}{D^3}\right)^{1/2}, \tag{3.16}$$

and the correlation between V_{hole}/D^3 and $t_{imp}/(D/c)$ is clearly shown in figure 11(*a*). A larger volume of trapped air inside the holes monotonically extends the impact duration. While $t_{imp}/(D/c)$ is approximately 3 for the flat disks ($V_{hole}/D^3 = 0$), it can increase up to 7 for the surface-patterned disks. Here, the theoretical curve for the surface-patterned disks underestimates the impact duration obtained from the experiment. This underestimation occurs because the impact force rises more moderately than predicted by the theoretical model as demonstrated in figure 9, and thus the theoretical impact duration serves as a lower bound for the experimental results. Regarding the time duration of the rise phase of the impact force (t_{rise} in figure 9), the values of the experimental measurements are greater than the theoretically predicted values, whereas they exhibit much less discrepancy for the time duration of the fall phase (t_{fall} in figure 9).

To further examine the relation between the impact duration and the volume of trapped air inside the holes, we selected three experimental models with $D = 50$ mm and different values of V_{hole}/D^3: figure 11(*b*) for $V_{hole}/D^3 = 0.008$ ($r = 2.8$ mm, $d = 3.2$ mm, $h = 2$ mm); figure 11(*c*) for $V_{hole}/D^3 = 0.018$ (1.8 mm, 8.2 mm, 2 mm); figure 11(*d*) for $V_{hole}/D^3 = 0.027$ (1.8 mm, 8.2 mm, 3 mm). We measured the time at which the volume of the air bubbles that had escaped from the holes near the centre of the disk after the depressurization process reached a maximum from the visualization images (figure 11*b–d*); $t/(D/c) = 0$ at the instant of impact. For the case of $V_{hole}/D^3 = 0.008$, it takes $t/(D/c) = 6.52$ for the trapped air to be vented. For the other values of $V_{hole}/D^3 = 0.018$ and 0.027, the venting of the trapped air is delayed: $t/(D/c) = 7.89$ and

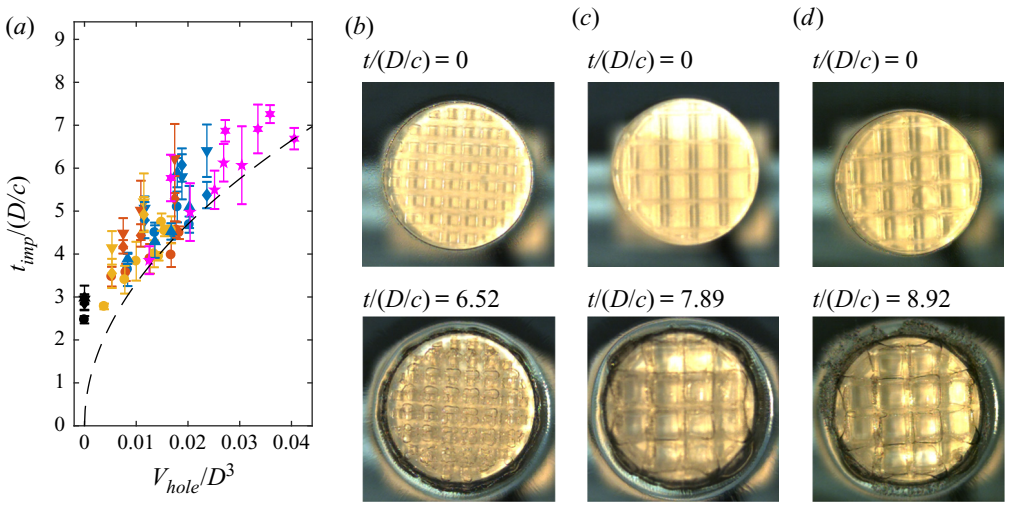

Figure 11. (*a*) Dimensionless impact duration $t_{imp}/(D/c)$ as a function of V_{hole}/D^3. The notation of the symbols is the same as in figure 4. The dashed line is given by (3.16). (*b–d*) Comparison of time at which the volume of the air bubbles that have escaped from the centre holes reaches a maximum for three surface-patterned disks with V_{hole}/D^3 = 0.008, 0.018 and 0.027, respectively ($D = 50$ mm and $U = 1.71\ \mathrm{m\,s^{-1}}$).

8.92, respectively. Although the time required for venting differs for each hole because of the non-uniform spatial distribution of pressure over the disk and the resultant spatial variation in the dynamics of air bubbles through the holes, a hole with a greater volume generally requires a longer time for the trapped air to be maximally vented. During the prolonged venting period, the trapped air inside the holes functions to cushion the impact, thereby extending the impact duration.

Using the intermediate parameter $t_{imp}/(D/c)$, we can now interpret the result in figure 4, where the increase in V_{hole}/D^3 leads to the monotonic decrease in $F_{max}/\rho_w cUA$. Neither the existence of the surface pattern nor its shape changes the magnitude of the impulse (figure 10*a*). Therefore, an extended impact duration would lead to a decrease in the maximum impact force because the impulse remains unchanged (figure 10*b*). Moreover, the amount of trapped air determines the impact duration (figure 11*a*). Increasing the volume of holes in the surface pattern allows more air to be trapped upon water impact, which extends the impact duration and subsequently reduces the maximum impact force (figure 4).

4. Concluding remarks

In this study, the water entry of a surface-patterned disk has been investigated to examine how the surface pattern affects the physical process of impact. During the initial phase, the sudden rise and fall of the impact force is synchronized with the compression and depressurization of the air bubbles trapped inside the holes that form the surface pattern. The air bubbles inside the holes contribute to a notable reduction in the peak impact force. The peak impact force is determined by the total volume of holes created by the surface pattern, and scales with $(V_{hole}/D^3)^{-1/2}$. The impulse imposed on the disk during the initial phase remains nearly constant for different disk diameters, irrespective of the volume and shape of the surface pattern. Because of the cushioning effect of the trapped air bubbles,

the impact duration of the surface-patterned disk is greater than that of the flat disk, and scales with $(V_{hole}/D^3)^{1/2}$.

For mechanical systems that plunge into the air–water interface or undergo slamming by water, a strong impact often causes structural damage. The results of this study suggest that the implementation of macroscale mesh-like surface patterns might be a practical approach for reducing this damage. In future work, we plan to investigate the effect of surface patterns on solid objects other than flat disks and explore their potential application in naval structures.

Supplementary movies. Supplementary movies are available at https://doi.org/10.1017/jfm.2021.123.

Funding. This research was supported by the Basic Science Research Program through the National Research Foundation of Korea (NRF) funded by the Ministry of Science and ICT (NRF-2020R1A2C2102232) and the Human Resources Program in Energy Technology of the Korea Institute of Energy Technology Evaluation and Planning (KETEP) granted financial resource from the Ministry of Trade, Industry and Energy, Republic of Korea (no. 20204030200050).

Declaration of interests. The authors report no conflict of interest.

Author ORCIDs.
Donghyun Kim https://orcid.org/0000-0002-2970-7320;
Daegyoum Kim https://orcid.org/0000-0002-7492-4631.

Appendix. Surface-patterned disks of arbitrary shapes

For surface-patterned disks, we experimentally and theoretically showed that $F_{max}/\rho_w cUA$ was determined by V_{hole}/D^3, regardless of the shape of the pattern (figure 4). To further support this result, we consider three types of surface patterns other than the regular square holes used throughout this study (figure 12*a*). The models were fabricated using the same procedure described in § 2, and the diameter of the disk and the depth of the pattern were kept constant at $D = 50$ mm and $h = 2$ mm. Type 1 is composed of regular triangular and hexagonal holes with different lengths and distances. Here, the definitions of d and r in figure 1(*b*) are used with the subscripts *tri* and *hex*. For the triangular holes, three models were manufactured using $d_{tri} = 3, 4, 5$ mm and $r_{tri} = 6.8, 5.1, 3.3$ mm, respectively. Likewise, three models with hexagonal holes were prepared: $d_{hex} = 6.4, 8.1, 10.4$ mm and $r_{hex} = 2, 3, 2$ mm, respectively. Type 2 contains rectangular holes of arbitrary sizes that are distributed randomly, and two models are presented in figure 12(*a*). Type 3 is a simple pattern that has a single round hole at the centre with a different hole diameter d_{round}. Four models were made using $d_{round} = 10, 20, 30, 40$ mm. For all models, the impact speed was set to be $U = 1.71\ \mathrm{m\,s^{-1}}$ by dropping the disks from $H = 15$ cm.

For types 1 and 2 with distributed holes, the maximum impact force coefficient $F_{max}/\rho_w cUA$ is in good agreement with the theoretical curve presented in figure 4 (figure 12*b*). Notably, even for type 3 with a single hole, the theoretical model can capture the general trend of the experimental results: monotonic decrease in $F_{max}/\rho_w cUA$ with V_{hole}/D^3. However, for type 3, $F_{max}/\rho_w cUA$ is distinctly smaller than the theoretically predicted value when $d_{round} = 10$ mm ($V_{hole}/D^3 = 0.0013$). When V_{hole}/D^3 is sufficiently large, the volume and cushioning effect of air inside the holes outweigh those of air inside the gap between the bottom surface of the pattern and the free surface, and the free-surface deformation is negligible. However, for the flat-disk case $V_{hole}/D^3 = 0$, the free-surface deformation just before the impact cannot be neglected, hence our theoretical model is not applicable to the flat disk. In the same way, for very small V_{hole}/D^3 cases, the effect

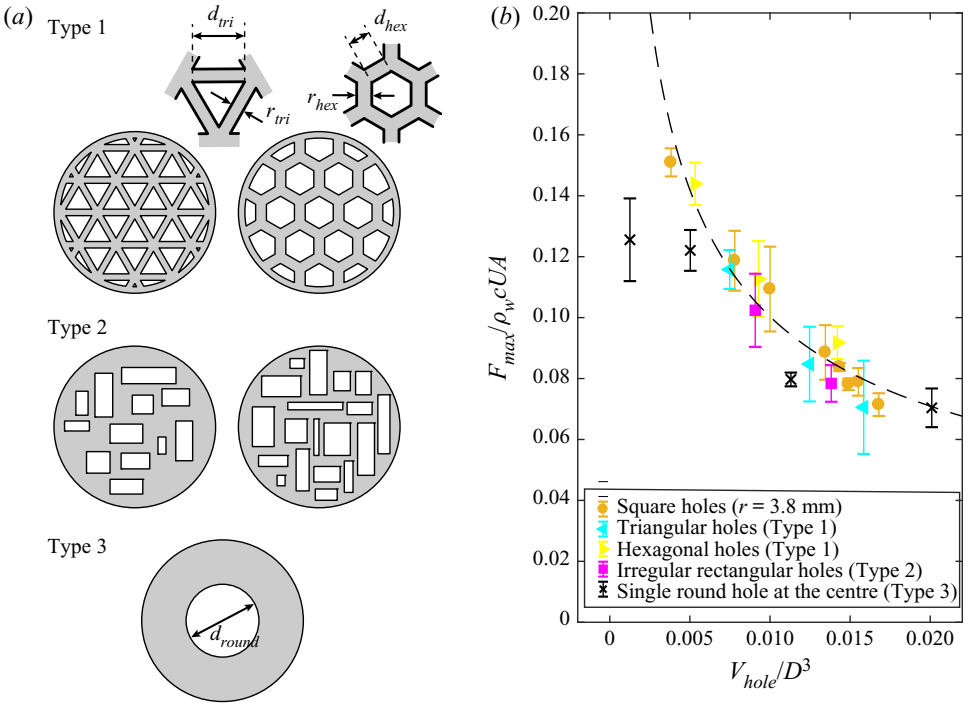

Figure 12. (*a*) Three types of surface patterns. All disks have the same $D = 50$ mm and $h = 2$ mm. (*b*) Maximum impact force coefficient $F_{max}/\rho_w cUA$ versus dimensionless total volume of holes V_{hole}/D^3 for the three pattern types. As a reference, disks with regular square holes ($r = 3.8$ mm) from figure 4 are included. The dashed line is given by (3.14).

of the free-surface deformation becomes important, and our theoretical model tends to overestimate the impact force.

In addition, one of the basic assumptions of our theoretical approach is that holes are distributed uniformly in the surface pattern and quantities such as pressure and penetration depth are uniform through the holes. Thus, in the intermediate range of V_{hole}/D^3, the single-hole cases with $d_{round} = 20$ and 30 mm ($V_{hole}/D^3 = 0.005$ and 0.011) exhibit a larger deviation from the theoretical curve, compared with the cases with distributed hole patterns with similar values of V_{hole}/D^3 (figure 12*b*). Meanwhile, the single-hole case with $d_{round} = 40$ mm ($V_{hole}/D^3 = 0.020$) shows the better agreement with the theoretical model. In this case, the hole diameter is so large that the disk has a narrow rim, which is similar to the disk in the inset of figure 4, and the assumption regarding the distributed hole pattern is valid.

References

Abrate, S. 2011 Hull slamming. *Appl. Mech. Rev.* **64** (6), 060803.

Aristoff, J.M & Bush, J.W.M. 2009 Water entry of small hydrophobic spheres. *J. Fluid Mech.* **619**, 45–78.

Bergmann, R., Van Der Meer, D., Gekle, S., Van Der Bos, A. & Lohse, D. 2009 Controlled impact of a disk on a water surface: cavity dynamics. *J. Fluid Mech.* **633**, 381–409.

Bodily, K.G., Carlson, S.J. & Truscott, T.T. 2014 The water entry of slender axisymmetric bodies. *Phys. Fluids* **26** (7), 072108.

Chang, B., Croson, M., Straker, L., Gart, S., Dove, C., Gerwin, J. & Jung, S. 2016 How seabirds plunge-dive without injuries. *Proc. Natl Acad. Sci. USA* **113** (43), 12006–12011.

CLIFTON, G.T., HEDRICK, T.L. & BIEWENER, A.A. 2015 Western and Clark's grebes use novel strategies for running on water. *J. Expl Biol.* **218** (8), 1235–1243.

CRANDELL, K.E., HOWE, R.O. & FALKINGHAM, P.L. 2019 Repeated evolution of drag reduction at the air–water interface in diving kingfishers. *J. R. Soc. Interface* **16** (154), 20190125.

DUEZ, C., YBERT, C., CLANET, C. & BOCQUET, L. 2007 Making a splash with water repellency. *Nat. Phys.* **3** (3), 180.

ERMANYUK, E.V. & GAVRILOV, N.V. 2011 Experimental study of disk impact onto shallow water. *J. Appl. Mech. Tech. Phys.* **52** (6), 889–895.

ERMANYUK, E.V. & OHKUSU, M. 2005 Impact of a disk on shallow water. *J. Fluids Struct.* **20** (3), 345–357.

FLOYD, S., KEEGAN, T., PALMISANO, J. & SITTI, M. 2006 A novel water running robot inspired by basilisk lizards. In *2006 IEEE/RSJ International Conference on Intelligent Robots and Systems*, pp. 5430–5436. IEEE.

FLOYD, S. & SITTI, M. 2008 Design and development of the lifting and propulsion mechanism for a biologically inspired water runner robot. *IEEE Trans. Robot.* **24** (3), 698–709.

GEKLE, S. & GORDILLO, J.M. 2010 Generation and breakup of worthington jets after cavity collapse. Part 1. Jet formation. *J. Fluid Mech.* **663**, 293–330.

GLASHEEN, J.W. & MCMAHON, T.A. 1996*a* A hydrodynamic model of locomotion in the basilisk lizard. *Nature* **380** (6572), 340.

GLASHEEN, J.W. & MCMAHON, T.A. 1996*b* Vertical water entry of disks at low froude numbers. *Phys. Fluids* **8** (8), 2078–2083.

HOWISON, S.D., OCKENDON, J.R. & WILSON, S.K. 1991 Incompressible water-entry problems at small deadrise angles. *J. Fluid Mech.* **222**, 215–230.

HSIEH, S.T. & LAUDER, G.V. 2004 Running on water: three-dimensional force generation by basilisk lizards. *Proc. Natl Acad. Sci. USA* **101** (48), 16784–16788.

HUERA-HUARTE, F.J., JEON, D. & GHARIB, M. 2011 Experimental investigation of water slamming loads on panels. *Ocean Engng* **38** (11–12), 1347–1355.

JALALISENDI, M., BENBELKACEM, G. & PORFIRI, M. 2018 Solid obstacles can reduce hydrodynamic loading during water entry. *Phys. Rev. Fluids* **3** (7), 074801.

JALALISENDI, M., SHAMS, A., PANCIROLI, R. & PORFIRI, M. 2015 Experimental reconstruction of three-dimensional hydrodynamic loading in water entry problems through particle image velocimetry. *Exp. Fluids* **56** (2), 41.

KAPSENBERG, G.K. 2011 Slamming of ships: where are we now? *Phil. Trans. R. Soc.* A **369** (1947), 2892–2919.

VON KÁRMÁN, T. 1929 The impact on seaplane floats during landing. *Tech. Rep.* 309313. National Advisory Committee on Aeronautics.

KOROBKIN, A. 2004 Analytical models of water impact. *Eur. J. Appl. Maths* **15** (6), 821–838.

KOROBKIN, A.A. & PUKHNACHOV, V.V. 1988 Initial stage of water impact. *Annu. Rev. Fluid Mech.* **20** (1), 159–185.

MA, Z.H., CAUSON, D.M., QIAN, L., MINGHAM, C.G., MAI, T., GREAVES, D. & RABY, A. 2016 Pure and aerated water entry of a flat plate. *Phys. Fluids* **28** (1), 016104.

MARSTON, J.O., TRUSCOTT, T.T., SPEIRS, N.B., MANSOOR, M.M. & THORODDSEN, S.T. 2016 Crown sealing and buckling instability during water entry of spheres. *J. Fluid Mech.* **794**, 506–529.

MATHAI, V., GOVARDHAN, R.N. & ARAKERI, V.H. 2015 On the impact of a concave nosed axisymmetric body on a free surface. *Appl. Phys. Lett.* **106** (6), 064101.

MAY, A. 1975 Water entry and the cavity-running behavior of missiles. *Tech. Rep.* NAVSEA Hydroballistics Advisory Committee.

MAYER, H.C. & KRECHETNIKOV, R. 2018 Flat plate impact on water. *J. Fluid Mech.* **850**, 1066–1116.

MOGHISI, M. & SQUIRE, P.T. 1981 An experimental investigation of the initial force of impact on a sphere striking a liquid surface. *J. Fluid Mech.* **108**, 133–146.

OKADA, S. & SUMI, Y. 2000 On the water impact and elastic response of a flat plate at small impact angles. *J. Mar. Sci. Technol.* **5** (1), 31–39.

RINGSBERG, J.W., HEGGELUND, S.E., LARA, P., JANG, B.-S. & HIRDARIS, S.E. 2017 Structural response analysis of slamming impact on free fall lifeboats. *Mar. Struct.* **54**, 112–126.

SHAMS, A., JALALISENDI, M. & PORFIRI, M. 2015 Experiments on the water entry of asymmetric wedges using particle image velocimetry. *Phys. Fluids* **27** (2), 027103.

SHAMS, A. & PORFIRI, M. 2015 Treatment of hydroelastic impact of flexible wedges. *J. Fluids Struct.* **57**, 229–246.

SIDDALL, R., ORTEGA ANCEL, A. & KOVAČ, M. 2017 Wind and water tunnel testing of a morphing aquatic micro air vehicle. *Interface Focus* **7** (1), 20160085.

SPEIRS, N.B., BELDEN, J., PAN, Z., HOLEKAMP, S., BADLISSI, G., JONES, M. & TRUSCOTT, T.T. 2019 The water entry of a sphere in a jet. *J. Fluid Mech.* **863**, 956–968.

THORODDSEN, S.T., ETOH, T.G., TAKEHARA, K. & TAKANO, Y. 2004 Impact jetting by a solid sphere. *J. Fluid Mech.* **499**, 139–148.

TRUSCOTT, T.T., EPPS, B.P. & BELDEN, J. 2014 Water entry of projectiles. *Annu. Rev. Fluid Mech.* **46**, 355–378.

TRUSCOTT, T.T., EPPS, B.P. & TECHET, A.H. 2012 Unsteady forces on spheres during free-surface water entry. *J. Fluid Mech.* **704**, 173–210.

VERHAGEN, J.H.G 1967 The impact of a flat plate on a water surface. *J. Ship Res.* **11** (04), 211–223.

VINCENT, L., XIAO, T., YOHANN, D., JUNG, S. & KANSO, E. 2018 Dynamics of water entry. *J. Fluid Mech.* **846**, 508–535.

WAGNER, H. 1932 Über stoß-und gleitvorgänge an der oberfläche von flüssigkeiten. *Z. Angew. Math. Mech.* **12** (4), 193–215.

WANG, J., FALTINSEN, O.M. & LUGNI, C. 2019 Unsteady hydrodynamic forces of solid objects vertically entering the water surface. *Phys. Fluids* **31** (2), 027101.

YARI, E. & GHASSEMI, H. 2016 Hydrodynamic analysis of the surface-piercing propeller in unsteady open water condition using boundary element method. *Intl J. Nav. Archit. Ocean* **8** (1), 22–37.

YETTOU, E.-M., DESROCHERS, A. & CHAMPOUX, Y. 2006 Experimental study on the water impact of a symmetrical wedge. *Fluid Dyn. Res.* **38** (1), 47.

ZHAO, R. & FALTINSEN, O. 1993 Water entry of two-dimensional bodies. *J. Fluid Mech.* **246**, 593–612.